AIAA JOURNAL
Vol. 40, No. 10, October 2002

Large Eddy Simulation of Shock/Boundary-Layer Interaction

Eric Garnier* and Pierre Sagaut†
ONERA, 92322 Châtillon, France
and
Michel Deville‡
Ecole Polytechnique Fédérale de Lausanne, CH-1015 Lausanne, Switzerland

Bidimensional interaction of an oblique shock with a plane plate has been studied numerically using large eddy simulation (LES) and compared with experimental data. This case represents an idealized model of bidimensional air intake and constitutes a challenge for compressible LES because shock and strong separation are considered. Numerically, a particular attention is given to spatial numerical scheme and to inflow conditions. Numerical results are in good quantitative agreement with experimental results, and LES can now be considered as a predictive tool for such physically complex flow. Mean and fluctuating longitudinal velocity are in very satisfactory agreement with experimental data. Nevertheless, cross term ($u'w'$) appears underestimated. The separated zone is correctly described, and LES can be used for fine study of the physic of such interaction. The dependence of the solution to numerical parameters is studied extensively. The effects of the size of the domain in the spanwise direction, of the resolution in the longitudinal direction, and the presence of a subgrid-scale model do not appear to be deciding.

I. Introduction

SHOCK/BOUNDARY-LAYER interaction is still an important problem for supersonic aircraft designers. Such phenomena plays an important role both for internal and external aerodynamic. These interactions can lead to an increase of drag, separation, and loss of performances. Moreover, unsteadiness of the shock produces strong constraints on the structure and noise, and it modifies local heat transfer. In air intakes these effects lead to loss of pressure recovery.

Principal characteristics of shock/boundary-layer interactions can be found in the reviews of Adamson and Messiter,[1] Delery and Marvin,[2] and Smits and Dussauge.[3] An extensive bibliographic effort has been performed by Settles and Dodson,[4] who have shown that experimental studies of interest for code validation are rare. Here, we limit our scope to two dimensional interactions. Three of these interactions are classically studied experimentally: these are the interaction of a shock with a compression ramp, with a bump, and with a plane plate. The latter is the less investigated. These interactions combine the effects of an adverse pressure gradient, curvature of streamlines, volumic compression, and separation. These phenomena are at the origin of a strong amplification of velocity fluctuations.

Most of the computations to date have been performed on compression ramp configurations. The first unsteady simulation has been attempted by David[5] using large eddy simulation (LES) followed by Hunt and Nixon[6] using very large eddy simulation (VLES). Adams[7] has recently carried out the first direct numerical simulation (DNS) of compression ramp. Other LES have been performed by Urbin et al.[8,9] using unstructured mesh. Reynolds-averaged numerical simulations (RANS) are usually considered of poor quality (despite the use of recent methods[10,11]). Distribution of pressure along the interaction zone and sometimes, mean velocity, can be correctly predicted (in particular with multiscale models[12]), but second-order statistics are always poorly represented. Following the analysis of Marshall and Dolling,[13] the main cause of inaccuracy is related to the low-frequency unsteadiness of the shock, which is not taken into account by RANS approaches.

To our knowledge, the case of the interaction of an oblique shock with a boundary layer developing on a plane plate has never been treated using LES. Such a case (which models an idealized bidimensional air intake) has been experimentally studied by the team of J. P. Dussauge at Institute de Recherche pour les Ecoulements Hors Equilibre (IRPHE). The results using laser Doppler anemometry (LDA) can be found in the Ph.D. dissertation of Deleuze,[14] and the results obtained with hot-wire anemometry (HWA) are available in the Ph.D. dissertation of Laurent.[15] This experimental configuration has been found interesting for a validation purpose. In effect, LES of compressible shocked flows is still a subject of research; improvements of numerical schemes are necessary because it has been found by Garnier et al.[16] that the numerical dissipation of some highly accurate numerical schemes [like essentially nonoscillatory (ENO) schemes] can exceed the physical dissipation associated to a subgrid-scale (SGS) model. Because the addition of a numerical dissipation cannot be avoided in shocked flows, it was found necessary to apply this dissipation locally using sensors able to distinguish a turbulent fluctuation from a shock. Such approach, derived from the work of Yee et al.,[17] has been presented in Ref. 18. The goal of this paper is then to validate LES with advanced computational methods recently developed for the treatment of compressible shocked flows in a experimentally well-described configuration.[14,15] LES has already been used to treat shock homogeneous turbulence interaction,[19,20] but, in the present case, physics of the interaction is richer, and the presence of wall introduces additional difficulties.

The paper is organized as follows. First, compressible LES equations are recalled, and the numerical method is described. In Sec. III the simulated configuration is presented, and different numerical test cases are defined. Section IV is devoted to comparisons between experimental and numerical results. The general conclusion is given in Sec. V.

II. Mathematical Model

A. Filtered Equations

In LES the large-scale field is computed directly from the solution of the filtered (local volume-averaged) Navier–Stokes equations, and the small-scale stresses are modeled. The SGS model then represents the effects of the small scales on the large-scale motions. In the first works in compressible LES, the energy equation was written in a nonconservative form (for example, see Ref. 21). Because the conservative form is necessary when computing flows

Received 3 January 2001; revision received 2 April 2002; accepted for publication 10 April 2002. Copyright © 2002 by the American Institute of Aeronautics and Astronautics, Inc. All rights reserved. Copies of this paper may be made for personal or internal use, on condition that the copier pay the $10.00 per-copy fee to the Copyright Clearance Center, Inc., 222 Rosewood Drive, Danvers, MA 01923; include the code 0001-1452/02 $10.00 in correspondence with the CCC.

*Senior Scientist, 29, Avenue de la Division Leclerc, B.P. 72; egarnier@onera.fr.
†Research Scientist, 29, Avenue de la Division Leclerc, B.P. 72; sagaut@onera.fr.
‡Professor, Laboratory of Computational Engineering; michel.deville@epfl.ch.

with embedded shocks, Lee[22] has recast the Favre-filtered system in such a way that the time-dependent integrated quantities remain computable. This implies the substitution of the filtered energy equation $\bar{E} = \bar{p}/(\gamma - 1) + \frac{1}{2}\bar{\rho}\widetilde{u_j u_j}$ by the exact transport equation of the computable energy

$$\breve{E} = \bar{p}/(\gamma - 1) + \tfrac{1}{2}\bar{\rho}\tilde{u}_j\tilde{u}_j \tag{1}$$

where $\bar{\phi}$ is a volume average of the flow variable ϕ; ϕ' is the fluctuating part of ϕ: $\phi' = \phi - \bar{\phi}$; $\tilde{\phi} = \overline{\rho\phi}/\bar{\rho}$ is the mass-weighted (Favre) average of ϕ; and ϕ'' is the fluctuation from $\tilde{\phi}$. In Eq. (1) p is the pressure, ρ the density, and u_j represents the velocity components. (Summation over repeated indices is assumed.) The specific heat ratio γ is classically set to 1.4. This approach was completed by Vreman et al.,[23] who took into account all of the SGS terms inherent to this formulation.

Once nondimensionalized with the mean inflow values of the density ρ_1, the velocity u_1, the temperature T_1, and a reference length L_1, the filtered Navier–Stokes equations for an ideal gas of constant R and specific heat ratio γ read, following Vreman et al.,[23]

$$\frac{\partial\bar{\rho}}{\partial t} + \frac{\partial\bar{\rho}\tilde{u}_j}{\partial x_j} = 0 \tag{2}$$

$$\frac{\partial\bar{\rho}\tilde{u}_i}{\partial t} + \frac{\partial}{\partial x_j}\bar{\rho}\tilde{u}_i\tilde{u}_j + \frac{\partial\bar{p}}{\partial x_i} - \frac{\partial\breve{\sigma}_{ij}}{\partial x_j} = -\frac{\partial}{\partial x_j}\tau_{ij} \tag{3}$$

$$\frac{\partial\breve{E}}{\partial t} + \frac{\partial}{\partial x_j}[(\breve{E} + \bar{p})\tilde{u}_j] - \frac{\partial}{\partial x_j}(\breve{\sigma}_{ij}\tilde{u}_i) + \frac{\partial\breve{q}_j}{\partial x_j} = -B_1 - B_2 - B_3 + B_4 + B_5 \tag{4}$$

$$\tilde{T} = \gamma Ma^2\frac{\bar{p}}{\bar{\rho}} \tag{5}$$

Once the subgrid-stress tensor

$$\tau_{ij} = \bar{\rho}(\widetilde{u_i u_j} - \tilde{u}_i\tilde{u}_j) \tag{6}$$

is introduced, the subgrid terms B_i read

$$B_1 = \frac{1}{\gamma - 1}\frac{\partial}{\partial x_j}(\overline{pu_j} - \bar{p}\tilde{u}_j) \tag{7}$$

$$B_2 = \overline{p\frac{\partial u_k}{\partial x_k}} - \bar{p}\frac{\partial\tilde{u}_k}{\partial x_k} \tag{8}$$

$$B_3 = \frac{\partial}{\partial x_j}(\tau_{kj}\tilde{u}_k) \tag{9}$$

$$B_4 = \tau_{kj}\frac{\partial}{\partial x_j}\tilde{u}_k \tag{10}$$

$$B_5 = \overline{\sigma_{kj}\frac{\partial}{\partial x_j}u_k} - \overline{\sigma_{kj}}\frac{\partial}{\partial x_j}\tilde{u}_k \tag{11}$$

SGS terms (not reported here) induced by the nonlinearity of the viscous stress and heat flux are found negligible by Vreman et al.[23] The computable stress tensor and heat flux read

$$\breve{\sigma}_{ij} = \frac{\mu(\tilde{T})}{Re}\widetilde{S}_{ij} \qquad \text{with} \qquad \widetilde{S}_{ij} = \frac{\partial\tilde{u}_i}{\partial x_j} + \frac{\partial\tilde{u}_j}{\partial x_i} - \frac{2}{3}\delta_{ij}\frac{\partial\tilde{u}_k}{\partial x_k} \tag{12}$$

$$\breve{q}_j = \frac{-\mu(\tilde{T})}{(\gamma - 1)Re\,Pr\,Ma^2}\frac{\partial\tilde{T}}{\partial x_j} \tag{13}$$

The molecular dynamic viscosity is given by the Sutherland law:

$$\mu(T) = T^{\frac{3}{2}}[(1 + C)/(T + C)] \tag{14}$$

where $C = 0.76$, which corresponds to a reference temperature of 144.6 K (see Sec. III for the reference values of the computation). The Prandtl number is fixed to 0.72.

B. SGS Modeling

The SGS tensor defined in Eq. (6) cannot be computed directly, and an SGS model has to be introduced to close the system of filtered equations. In this study, the mixed-scale model (MSM)[24] has been considered because it performs well for wall-bounded flows as demonstrated by Lenormand et al.,[25,26] and its computational cost is low. Its behavior was also demonstrated to be satisfactory for shock/homogeneous turbulence interaction by Garnier et al.[20] Nevertheless, the use of models based on eddy-viscosity assumption is not completely qualified for shock/turbulence interaction. This model can be written as follows:

$$\tau_{ij} - \tfrac{1}{3}\tau_{kk}\delta_{ij} = -\bar{\rho}\nu_t\tilde{S}_{ij} \tag{15}$$

with

$$|\widetilde{S}^*| = \left(2\widetilde{S}^*_{ij}\widetilde{S}^*_{ij}\right)^{\frac{1}{2}}$$

where $\widetilde{S}^*_{ij} = \frac{1}{2}(\partial\tilde{u}_i/\partial x_j + \partial\tilde{u}_j/\partial x_i)$, the filter length scale is evaluated as $\Delta = (\Delta x\Delta y\Delta z)^{1/3}$. The isotropic part of the SGS tensor is supposed to be negligible as in Ref. 27. These authors have not considered cases with shocks. Moreover, it is worth stressing that in shock regions the numerical diffusion is expected to overcome the diffusion of the SGS model.

In the energy equation the term B_1 is modeled as

$$B_1 = \frac{-\bar{\rho}\nu_t}{(\gamma - 1)Ma^2Pr_t}\frac{\partial\tilde{T}}{\partial x_i} \tag{16}$$

with a turbulent Prandtl number Pr_t equal to 0.9.

The SGS viscosity of the MSM reads

$$\nu_t = C_m|\widetilde{S}^*|^\alpha\left(q_c^2\right)^{(1-\alpha)/2}\Delta^{(1+\alpha)} \tag{17}$$

with

$$q_c^2 = \tfrac{1}{2}(\tilde{u}_k - \hat{\tilde{u}}_k)^2$$

The test filter $\hat{}$ is derived from the trapezoidal rule, α is set to 0.5, and consequently the parameter $C_m = C_m(\alpha)$ is found equal to 0.06 on the assumption of equilibrium between dissipation rate and energy transfer rate in homogeneous isotropic turbulence. This model is presented as a low computational cost alternative to dynamic models because it simply takes into account the local structure of the flow by computing the kinetic energy of the highest resolved frequencies q_c^2.

The behavior of this model can be improved[25,28] using a selection function that multiplies the SGS viscosity. This function (from David[5]) tests the tridimensionality of the flow, which is a characteristic of turbulent flows. In the initial version of David, a boolean operator commands the local application of SGS viscosity. Sagaut and Troff[28] have derived a smoother function:

$$f_{\theta_0}(\theta) = \begin{cases} 1 & \text{if} \quad \theta \geq \theta_0 \\ r(\theta)^n & \text{elsewhere} \end{cases} \tag{18}$$

The angle θ is given by the following relation:

$$\theta = \arcsin\left(\frac{\|\hat{\omega}\times\omega\|}{\|\hat{\omega}\|\cdot\|\omega\|}\right) \tag{19}$$

where ω is the vorticity and $\hat{\omega}$ its local filtered value.

The function r is defined as

$$r(\theta) = \frac{\tan^2(\theta/2)}{\tan^2(\theta_0/2)} \tag{20}$$

the exponent n is chosen equal to 2 and $\theta_0 = 20$ deg.

In this study B_2 is neglected for all SGS models as in Moin et al.[29] and Erlebacher et al.[27] The term B_5 is neglected as in Ref. 22, and once τ_{ij} is modeled B_3 and B_4 can be computed explicitly.

C. Numerical Scheme

The numerical scheme is based on nonlinear weighted ENO (WENO) filters defined in Ref. 18. The basis of this scheme, derived from the work of Yee et al.,[17] is now described.

Let U^n denote the vector of the conservative variables evaluated at the time $n\Delta t$ and Δt be the time step and $\hat{U}^{(n+1)}$ the vector of the conservative variables after the application of any explicit time-integration scheme. This vector is spatially filtered to give the final state $U^{n+1}\{U^{n+1} = \mathcal{F}[\hat{U}^{(n+1)}]\}$. The main point is that the time advancement is performed with a nondissipative spatial operator (noted L). The filtering pass is decomposed as follows:

$$U^{(n+1)} = \mathcal{F}\left[\hat{U}^{(n+1)}\right] = (I_d + \beta\Delta t L_f)\left[\hat{U}^{(n+1)}\right] \tag{21}$$

where L_f is any dissipative operator, I_d is the identity, and the switch β is defined as

$$\begin{cases} \beta = 0 & \text{if} \quad \Psi < \epsilon \\ \beta = 1 & \text{if} \quad \Psi \geq \epsilon \end{cases} \tag{22}$$

where Ψ is the sensor of Ducros et al.[19] defined as

$$\Psi = \frac{[\mathrm{div}(\boldsymbol{u})]^2}{[\mathrm{div}(\boldsymbol{u})]^2 + [\mathrm{rot}(\boldsymbol{u})]^2} \tag{23}$$

where $\boldsymbol{u}$ denotes the velocity vector. This sensor, which was originally developed to be used in conjunction with the classical Jameson sensor, was demonstrated to be able to distinguish a turbulent fluctuation from a shock in Refs. 18 and 19.

In this study the time integration is performed by means of a third-order-accurate total-variation-diminishing (TVD) Runge–Kutta method proposed by Shu and Osher[30]:

$$\begin{aligned} U^{(1)} &= U^n + \Delta t L(U^n) \\ U^{(2)} &= \tfrac{3}{4}U^n + \tfrac{1}{4}U^{(1)} + \tfrac{1}{4}\Delta t L\left[U^{(1)}\right] \\ \hat{U}^{(n+1)} &= \tfrac{1}{3}U^n + \tfrac{2}{3}U^{(2)} + \tfrac{2}{3}\Delta t L\left[U^{(2)}\right] \end{aligned} \tag{24}$$

Note that L is referred to as "base scheme" and can be any qth-order-accurate finite volume or finite difference nondissipative scheme.

As mentioned by Yee et al.,[17] L_f can be the dissipative part of any shock-capturing scheme and can be expressed as follows in a monodimensional case:

$$L_f\left[\hat{U}^{(n+1)}\right] = L_f(F^*, G^*) = (1/\Delta x)\left(F^*_{i+\frac{1}{2},j} - F^*_{i-\frac{1}{2},j}\right) \tag{25}$$

where $F^*_{i+1/2,j}$ is dissipative numerical flux for the filter operator. Such an operator is derived of ENO schemes.

The dissipative part of the ENO scheme is obtained by subtracting a mth-order-accurate centered scheme to an rth-order-accurate ENO scheme:

$$F^{\mathrm{eno}}_{i+\frac{1}{2},j} = R_{i+\frac{1}{2}}\Phi_{i+\frac{1}{2}} \tag{26}$$

with

$$\phi^l_{i+\frac{1}{2}} = \left(\sum_{p=0}^{r-1} \vartheta^r_{k,p} R^{-1}_{i+\frac{1}{2}} F_{i-r+1+k+p} - \sum_{p=0}^{m-1} \vartheta^m_{m/2,p} R^{-1}_{i+\frac{1}{2}} F_{i-m+1+m/2+p}\right) \tag{27}$$

where $\vartheta^r_{k,p}$ are the reconstruction coefficients (given in Ref. 31) of the ENO procedure, and k is the stencil index selected among the r candidate stencils. This stencil, called S_k, is defined as

$$S_k = (x_{i+k-r+1}, x_{i+k-r+2}, \ldots, x_{i+k}), \qquad k = 0, \ldots, r-1 \tag{28}$$

The matrices $R_{i+1/2}$ (respectively, $R^{-1}_{i+1/2}$) are the left (respectively, right) eigenvectors matrices of $\partial F/\partial U$ evaluated using a Roe mean.

The mth-order-accurate centered scheme is a particular subclass of ENO scheme with the stencil index k of the reconstruction coefficient $\vartheta^m_{k,p}$ set to $m/2$. Obviously, the order of the centered scheme m is even. Whatever the value of $m \geq 2$, this method allows the exhibition of the dissipative terms of the truncation errors. Nonetheless, to keep the precision of the base scheme it is necessary to choose $m = q$. A larger value of m does not improve the formal global precision.

To increase the order of accuracy with respect to ENO filters, WENO filters can be derived:

$$\phi^l_{i+\frac{1}{2}} = \sum_{k=0}^{r-1} \omega_k \left[\left(\sum_{p=0}^{r-1} \vartheta^r_{k,p} R^{-1}_{i+\frac{1}{2}} F_{i-r+1+k+p} - \sum_{p=0}^{m-1} \vartheta^m_{m/2,p} R^{-1}_{i+\frac{1}{2}} F_{i-m+1+m/2+p}\right)\right] \tag{29}$$

The WENO approach[31] consists in performing linear combinations of the r possible rth-order ENO fluxes. The weights ω_k adapt themselves to the relative smoothness of the flow on each candidate stencil, in such a way that the stencils which contain a discontinuity are assigned a nearly zero weight. In absence of discontinuity, the choice of optimal weights allow the increase of the order of accuracy of the WENO schemes up to $(2r-1)$th order of accuracy. The procedure used to compute the ω_k is described by Jiang and Shu.[31] The ENO schemes are combined with a Roe solver for all of the results presented here.

In this study we have used a combination of a fourth-order-centered base scheme with a fifth-order-accurate WENO filter. The threshold ϵ is fixed to 0.04. In practice, this method limits the computation of the filter to about 20% of the total number of grid points.

Viscous fluxes are discretized by means of a second-order-accurate-centered scheme. The Courant–Friedrichs–Lewy (CFL) number is fixed to 0.5.

III. Description of the Configuration

A. Experimental Setup

The shock is generated by a corner fixed to the upper plate of the wind tunnel and interacts with the turbulent boundary layer, which develops on the lower plate. In this study we chose to use the data available for a corner angle of 8 deg, which can generate a shock strong enough to produce a separation of the boundary layer. The lower plate of the wind tunnel is assumed to be adiabatic.

B. Computational Parameters

The length of the computational domain is restricted to the measurement zone. (It begins at $x = 252$ mm and ends at $x = 440$ mm.) The height of the domain is 70.7 mm, whereas the height of the wind tunnel is 120 mm. The computational domain is presented in Fig. 1. (Note that the axis x denotes the longitudinal direction, y the spanwise direction, and z the wall-normal direction.) The width of the computational domain is about 15 mm in the spanwise direction (for the test cases A, C, and D), whereas the wind tunnel is 10 times larger.

At the inflow (at $x = 252$ mm) the temperature T_e outside of the boundary layer is 144.6 K, the density ρ_e is equal to 9.66×10^{-2} kg/m^3, and the velocity value U_e is 557 m/s. With these conditions the Mach number is equal to 2.3. The reference length chosen in those computations is the measured displacement length δ_1, which is equal to 3.535 mm at $x = 260$ mm. This length is defined as

$$\delta_1 = \int_0^\infty \left(1 - \frac{\rho u}{\rho_e U_e}\right) \mathrm{d}z \tag{30}$$

The Reynolds number $Re(\delta_1)$ based on the displacement length U_e, ρ_e, and $\mu(T_e)$ is equal to 19,132.

In this study four simulations have been carried out in order to check the sensitivity of the results to computational details. The characteristic of these simulations are reported in Table 1. The numbers of grid points (N_x, N_y, N_z) in each direction are mentioned, and the size of the computational meshes (Δ_x^+, Δ_y^+, Δ_z^+) are given in wall units $\{z^+ = (u_\tau/\nu_w)z$, where the friction velocity is defined as $u_\tau = \sqrt{[(\mu_w/\rho_w)(\partial\langle u\rangle/\partial z)_w]}$ and ρ_w and μ_w are, respectively, the density and the viscosity at the wall$\}$. These wall units are based on an experimentally measured friction velocity of 24.75 m/s at

$x = 260$ mm. Test case A is the base case. In test case B the influence of a doubling of the domain size in the spanwise direction is investigated. The effect of a refined grid in the longitudinal direction is studied using case C, and case D is devoted to the investigation of the SGS model contribution. The resolution reported in Table 1 can be compared with the one used in DNS by Adams[7] ($\Delta_x^+ = 6$, $\Delta_y^+ = 3.2$ at the inflow plane) and by Guarini et al.[32] ($\Delta_x^+ = 8.9$, $\Delta_y^+ = 5.9$).

The distribution of grid points follows an hyperbolic tangent law in the wall-normal direction. At the inflow there are 16 points between the wall, and the ordinate z^+ equals 30. The mesh is regular in directions x and y. Periodic boundary conditions are applied in the spanwise direction. Nonreflective conditions[33] are applied on the upper frontier. At the outflow a 13-mm-long sponge zone ensures the damping of turbulent fluctuations, which are evacuated by means of nonreflective conditions. This method was successfully used in Ref. 7. No-slip and adiabaticity conditions are applied on the wall. The pressure gradient is computed by means of a projection of Navier–Stokes equations in the wall-normal direction.

The generation of realistic inflow conditions is a very sensitive issue in LES. In this study we followed the methodology introduced by Lund et al.[34] and extended to compressible flow by Urbin and Knight.[35] Using this strategy, the simulation generates its own inflow conditions through a sequence of operations where the flowfield at a downstream station is rescaled and reintroduced at the inflow boundary. The general idea is to decompose each flowfield component into a mean and fluctuating part and then to apply the appropriate scaling law to each part separately. It is then possible to prevents the thickening of the boundary layer by fixing target values of friction velocity and momentum thickness. The inhomogeneity caused by the presence of shock requires the Lund procedure to be applied on a second simulation of time-developing canonical turbulent boundary layer. An $x = cste$ plane of this second simulation is extracted and introduced in the shock/boundary-layer LES inflow plane at each time step.

Once given the angle of the incident shock and inflow conditions, Rankine–Hugoniot relationships allow the computation of the fluid state between incident shock and reflected shock (Fig. 1). In the absence of boundary layer, the incident shock impacts the plate at $x = 336$ mm, and this angle with respect to the plate is 32.41 deg.

Statistics are the results of a mean process in time and in the homogeneous direction y. First, 300,000 time steps are computed. This time corresponds to 18 flow-through times (FTT) of the computational box for a fluid particle transported at the velocity U_e. This time is necessary to get the correct position of the system incident shock/reflected shock. The turbulent field obtained for the case A is used to initialize cases B (with duplication in the direction y), C (with interpolation in the direction x), and D. Then, the means are performed on 84,000 time steps corresponding to five FTT.

Table 1 Computational parameters of the four test cases

Case	N_x	N_y	N_z	Δ_x^+	Δ_y^+	Δ_z^+, min	SGS model
A	255	55	151	50	18	1	Yes
B	255	110	151	50	18	1	Yes
C	510	55	151	25	18	1	Yes
D	255	55	151	50	18	1	No

IV. Analysis of the Results

The experience is particularly documented at $x = 260$ mm upstream of the interaction zone and at $x = 345$, 380, and 420 mm downstream of the interaction zone. Some data are available in the interaction zone. The maximal experimental uncertainties are lower than 10% for $z/\delta > 0.1$ and outside of the interaction zone. In particular, this value can be reached for the normal velocity fluctuations. All of the LES quantities presented in this section are time- and spanwise-averaged.

A. Inflow Plane

Classically when dealing with compressible flow, the mean velocity profiles are compared using a Van Driest transformation:

$$U_{\mathrm{VD}} = \int_0^{\langle u^+ \rangle} \sqrt{\frac{\langle \rho \rangle}{\langle \rho_w \rangle}}\, d\langle u^+(z^+) \rangle \qquad \text{with} \qquad \langle u^+ \rangle = \frac{\langle u \rangle}{\langle u_\tau \rangle} \tag{31}$$

The Van Driest transformed inflow mean velocity profiles are represented in Fig. 2. Computations and wind-tunnel experiments exhibit the expected logarithmic zone of equilibrium boundary layers. The experimental friction is not measured but evaluated assuming the profile follows the classical law $\ell n(z^+)/0.41 + 5.25$. This explains the perfect agreement of the experimental profile with this

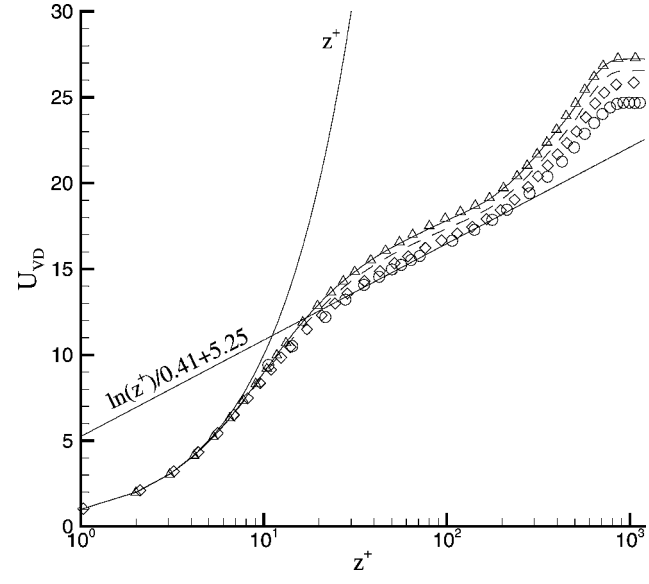

Fig. 2 Mean velocity profile at the inflow plane: ——, case A; △, case B; – – –, case C; ◇, case D; and ○, HWA.

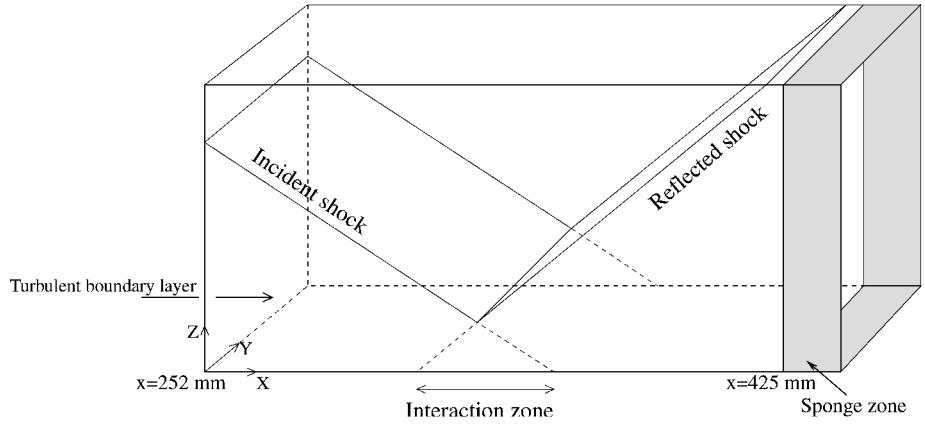

Fig. 1 Computational domain.

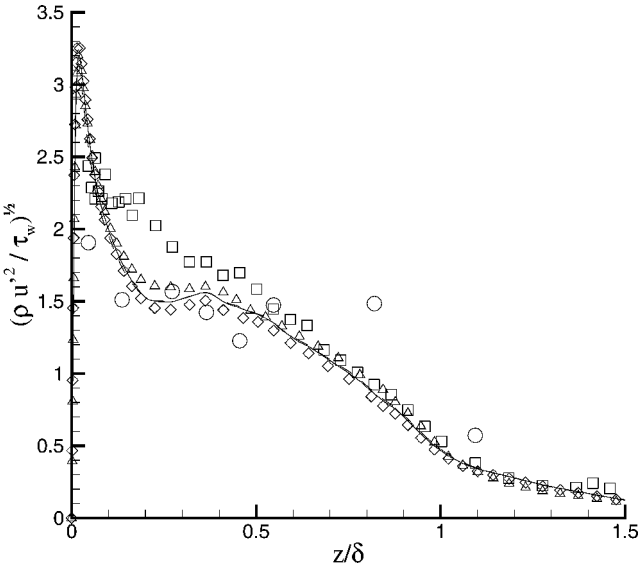

Fig. 3 Longitudinal velocity fluctuations profiles at the inflow plane: ——, case A; △, case B; – – –, case C; ◇, case D; □, LDA; and ○, HWA.

law. The discrepancies between the computations are very small, but the normalization of velocity per u_τ (which is very sensitive to the near wall dynamic of the flow) emphasizes them. As in the LES of Spyropoulos and Blaisdell,[36] our computations underestimate the wall friction (by about 10% for the less accurate cases A and B). The higher resolution of the test case C yields smaller error on the friction velocity than the other cases and appears to be closer to the experimental results than cases A and B. For the same reasons case D (without any model) yields the best results, but we will see later that the larger value of the friction is caused by an overestimation of turbulent fluctuations in the zone near the wall.

Following the work of Morkovin,[37] longitudinal velocity fluctuations are multiplied by density and adimensionalized by the friction velocity. This allows us to take into account the effects of kinetic heating (Mach-number effect) and to compare compressible and incompressible data. This change of variable is used in Fig. 3. Discrepancies between LDA and HWA data are noticeable in particular near $z/\delta \sim 0.1$ (where δ is the local boundary-layer thickness). Despite some experimental bias, former measurements on a shock-free boundary layer at the same Mach number have convinced Eléna and Lacharme[38] to agree on the superiority of LDA measurements. Unfortunately, our numerical results as those presented in the Ref. 36 are in better agreement with experimental results obtained using HWA. In the near-wall region (not documented experimentally) velocity fluctuations levels are the same as those obtained using LES by Spyropoulos et Blaisdell[36] on the one hand and by Urbin et al.[8] (for a Mach number of 2.9) on the other hand. The maximum of fluctuations reaches 3.2 in the three cases. Fluctuations obtained for case D are slightly overestimated with respect to other cases. This overestimation is customary for computations performed without any SGS model; Kravchenko and Moin[39] observe the same tendency in incompressible plane channel computations. Moreover, the amplitude of this overestimation is here minimized by the normalization by u_τ. Without this artifact it reaches about 10%. One can remark a slope breaking near $z/\delta = 0.3$ in velocity fluctuation profiles of the computations. This one is absent of experimental data and of the numerical results presented in Ref. 36 but can be found to a lesser extend in Urbin et al.[8] computations. This slope breaking can be explained by the posttransitional behavior of the temporal boundary layer, which is imposed at the inflow boundary. This one is less marked in case B (initialized with a temporal simulation two times larger in the spanwise direction).

B. Description of the Interaction Region

First, isovalues of the mean pressure are presented in Fig. 4. The incident shock (which would impact near $x = 336$ mm in absence of boundary layer) curves penetrate the boundary layer (thickness

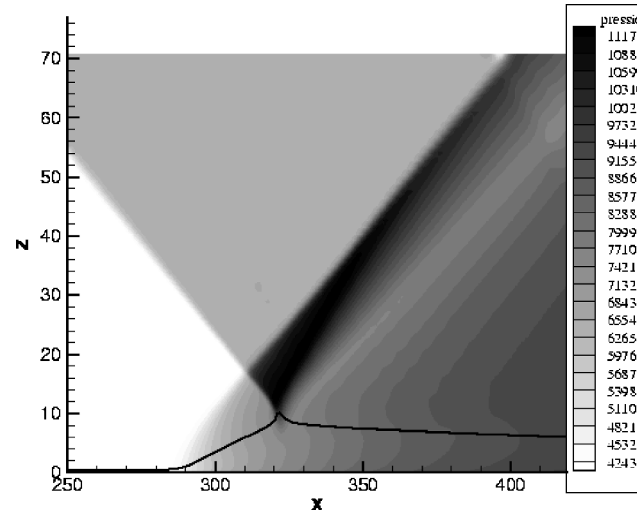

Fig. 4 Isovalues of the mean pressure and sonic line (in black).

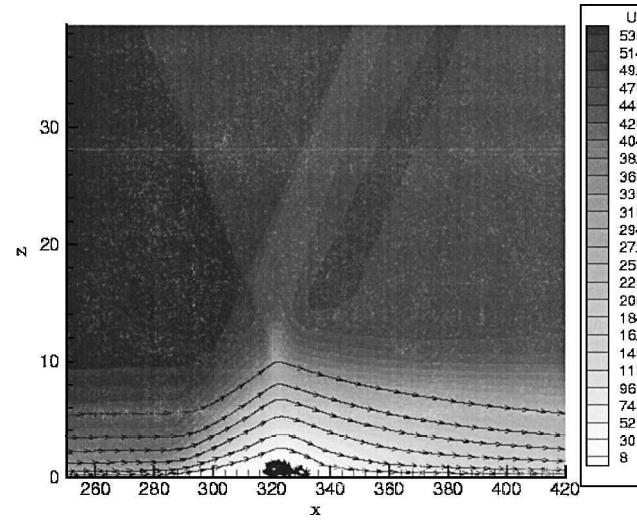

Fig. 5 Isovalues of the mean longitudinal velocity fluctuations.

of 11 mm at the inflow) and reflect on the sonic line as an expansion fan. The compression related to the rising of pressure waves in the subsonic part of the boundary layer focuses to form a reflected shock (where the trace begins in the vicinity of the position $x = 290$ mm at the wall). The continuation of this shock would impact on the wall near $x = 275$ mm and marks the beginning of the interaction zone.

Figure 5 displays isovalues of the longitudinal velocity field of case A. Streamlines are also represented. They clearly show the deviation undergone by the velocity fields in the interaction zone (between the continuation of incident and reflected shocks). The fluid is firstly deviated upward (up to $x = 320$ mm) and then downward. In this zone the flow is separated in agreement with the experimental observations.[15] In this work Laurent formulates the hypothesis that oscillations of the separation bubble govern those of the reflected shock and lead to a gain of energy in the low frequencies.

Isovalues of longitudinal velocity fluctuations are shown in Fig. 6. Upstream of the interaction, these fluctuations are strong in the near-wall region. One can observe that the fluctuations are amplified by a factor of two under the reflected shock (near $x = 290$ mm). The explanation given by Laurent[15] to explain this amplification of the fluctuations is a linear effect by rapid distorsion. The zone concerned by a high level of fluctuation spreads above the separated zone (near $x = 320$ mm; see Fig. 5). In agreement with experimental observations, one can notice an alignment of the isovalue lines of the fluctuations just downstream of the reflected shock. Downstream of the interaction zone, longitudinal and vertical (not shown) fluctuations are maximum in the middle of the boundary layer ($z/\delta \sim 0.6$).

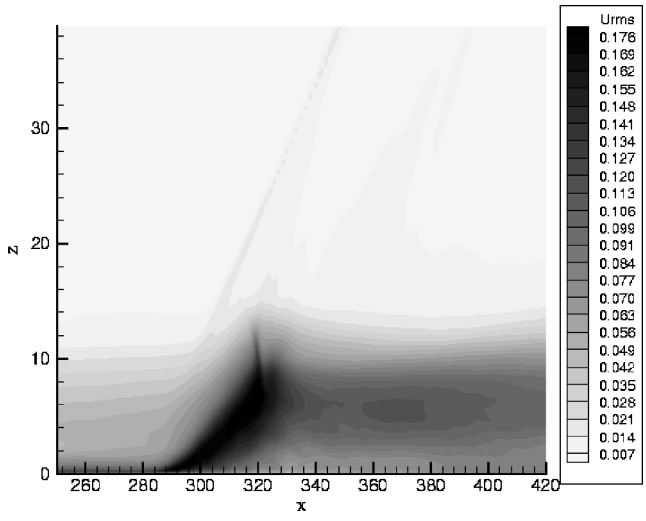

Fig. 6 Isovalues of the mean longitudinal velocity fluctuations.

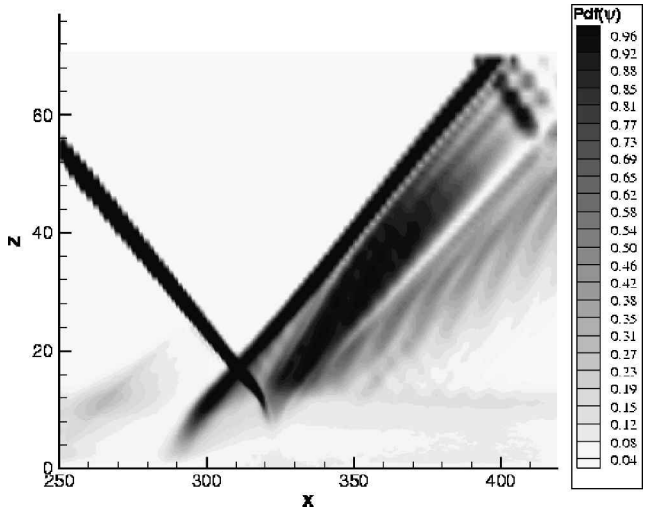

Fig. 7 Isovalues of the mean probability density function of Ducros sensor.

However, one can observe a second extremum of longitudinal fluctuations in the near-wall region close to the outflow; this is evidence of a (slow) return toward an equilibrium state. Particular attention must be paid to the interpretation of data concerning the fluctuations in the interaction zone because the unsteadiness of the shocks and of the recirculation bubble can be at the origin of a part of the fluctuations. (It is then not possible to consider turbulent fluctuations.) However, one must note that the thickness of the separation bubble is lower than 2 mm, excluding the contribution of its oscillations to the strong level of fluctuations observed in the middle of the boundary layer.

Independent of the analysis of the results concerning physical variables, we verify in Fig. 7 that the Ducros et al.[19] sensor applies nearly exclusively in the zone where we have noticed in Fig. 4 the presence of shock or expansion. Consequently, the SGS model is effective in most parts of the boundary layer. (Its effect is not masked by numerical dissipation.) Nevertheless, one can observe low values of the sensor on the upper limit of the boundary layer where the adaptation of the inflow conditions might not be perfect. Even if this strategy of minimization of the numerical dissipation would require further validation (see also Ref. 18) on different test cases, results presented here allows us to be confident with this concept.

C. Longitudinal Evolution

Longitudinal evolution of the displacement thickness is displayed in Fig. 8. The computation of this integral quantity is not trivial because the external velocity $U_e(x)$ varies in the longitudinal direction. The potential flow is supposed to be reached when the Ducros et al.[19] sensor value exceeds 0.1. This method gives results coherent with measurement because the value of δ_1 at the inflow of the computational domain is correctly predicted (at $x = 260$ mm) after a short transient. The evolution of δ_1 in the interaction zone (290 mm $< x <$ 340 mm) will not be commented in absence of corresponding experimental data. Looking at Fig. 8, one can observe that the displacement thickness is multiplied by a ratio larger than two during the interaction. This amplification rate is well predicted by computations and during the relaxation phase; where δ_1 decreases, the discrepancies do not exceed 10%.

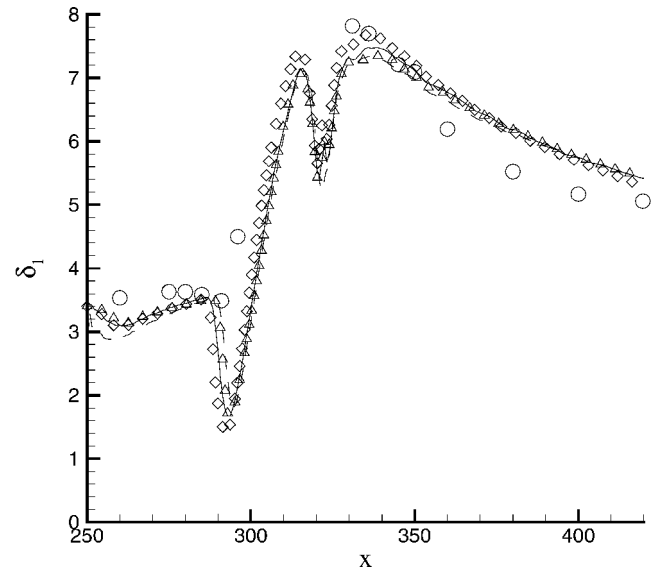

Fig. 8 Longitudinal evolution of the displacement thickness: ——, case A; △, case B; – – –, case C; ◇, case D; and ○, HWA.

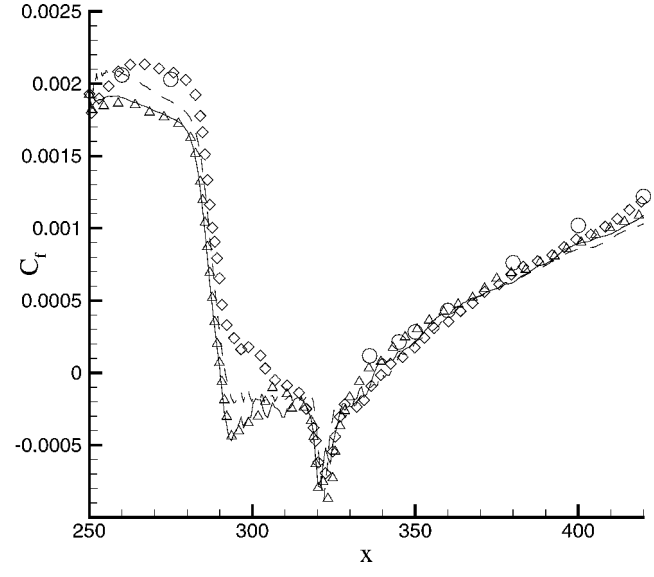

Fig. 9 Longitudinal evolution of friction coefficient: ——, case A; △, case B; – – –, case C; ◇, case D; and ○, HWA.

The longitudinal evolution of the friction coefficient is presented in Fig. 9. This coefficient is defined as

$$C_f = 2\mu_w \frac{(\partial \langle u \rangle / \partial z)_w}{\left[\rho_e(x) U_e(x)^2\right]} \tag{32}$$

At the inflow the discrepancies on the C_f between computations and experience are lower than 10% for cases A and B. (Such a kind of underestimation is classical with LES.[36]) Cases C (with the best resolution) and D give levels of C_f very close to the experiment. The flow is seen to be separated for cases A, B, and C

between $x = 290$ and 340 mm. The quasi-totality of the interaction zone is concerned by the separation. For case D the velocity fluctuations in the near-wall zone are stronger, and the flow separates later (near $x = 305$ mm). Furthermore, the intensity of the separation is lower for case C than for cases A and B between $x = 290$ and 315 mm; one can then observe an effect of the improved resolution in the x direction. Just after the interaction zone experimental evaluations based on hypothesis of existence of a logarithmic zone lead to a friction coefficient clearly positive at the opposite of the computations. In the relaxation zone the increase of C_f between computations and experiment is very similar, and at the outflow the discrepancies are comparable to those observed at the inflow (about 10%). One can notice that the results quality of LES is clearly superior to the one obtained with RANS approach (see Ref. 11 for a recent reference) in the same configuration (but at $Ma = 2.9$).

D. Comparisons Downstream of the Interaction

The point of impact of the incident shock varies if one uses data from jump relationship (as Deleuze[14] who found an impact at 330 mm) or extrapolation of schlieren visualization (as Laurent[15]). Here, the second choice has been performed, but we will see that the first choice would have been better. As a consequence, experimental data at $x = 345$ mm are compared with numerical data 6 mm downstream. To evaluate the influence of this modification, results for the case A are reported for abscissa corresponding to experimental data ($x = 345$ mm). At $x = 420$ mm this translation is not possible because the abscissa $x = 426$ mm belongs to the sponge zone. Nevertheless, consequences of this (low amplitude) translation are supposed to be negligible far from the interaction zone. Figures 10 and 11 display mean longitudinal velocity profiles for stations $x = 345$ and 420 mm, respectively.

The station $x = 345$ mm is located very close to the interaction zone end, and results for cases A and B are in good agreement with measurements, whereas cases C and D underestimate the velocity near $z/\delta = 0.1$. This underestimation is related to a recirculation zone that spread farther downstream in this both cases (see Fig. 9). Data for case A at $x = 345$ and 351 mm allow us to notice the improvement caused by the offset of 6 mm. At $x = 420$ mm differences between computations and experience are not negligible. Those discrepancies might be caused by the proximity of the sponge zone. In general, the best agreement is obtained with the case B followed by cases A, C, and D. It is possible that the absence of SGS model delays the relaxation. In effect, the diffusion associated to the model is supposed to favor the redistribution of kinetic energy from the middle of the boundary layer toward the wall.

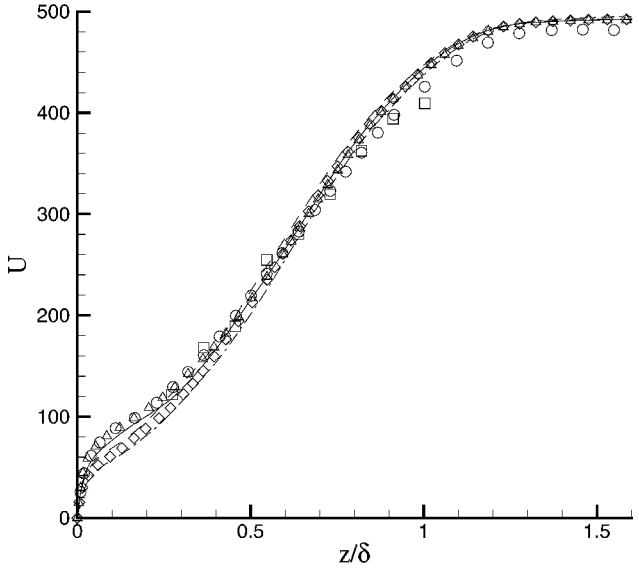

Fig. 10 Mean longitudinal velocity profiles. At x = 351 mm: ——, case A; △, case B; – – –, case C; and ◇, case D. At x = 345 mm: –·–, case A; ○, HWA; and □, LDA.

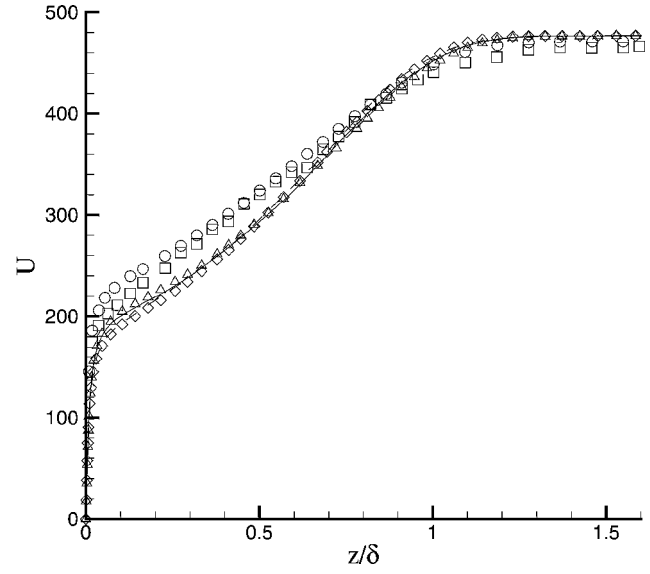

Fig. 11 Mean longitudinal velocity profiles at x = 420 mm: ——, case A; △, case B; – – –, case C; ◇, case D; ○, HWA; and □, LDA.

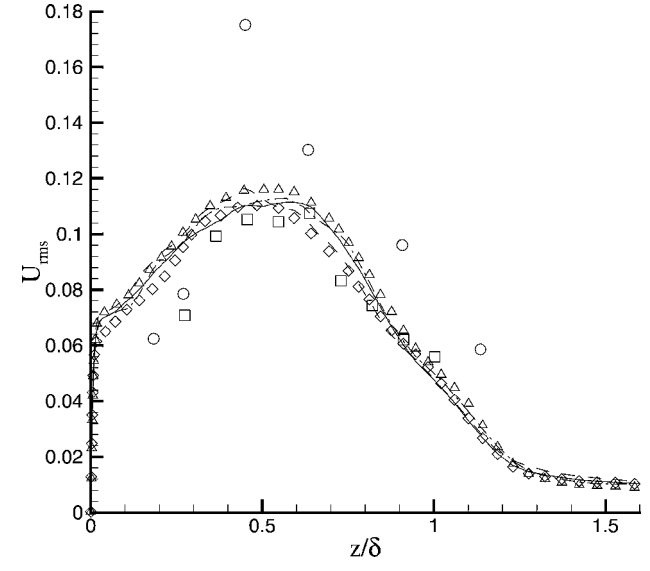

Fig. 12 Mean longitudinal velocity fluctuations profile. At x = 351 mm: ——, case A; △, case B; – – –, case C; and ◇, case D. At x = 345 mm: –·–, case A; ○, HWA; and □, LDA.

Longitudinal velocity fluctuations are plotted in Figs. 12 and 13 for stations $x = 345$ and 420 mm, respectively. Just after the interaction (Fig. 12), measurement difficulties are significant, and data obtained with HWA diverge from those obtained with LDA. Experimentalists favor the last method that is known to be more reliable in this kind of situation. Computations slightly underestimate velocity fluctuations for the two considered stations. The most important discrepancies are registered in the near-wall region where metrology difficulties are met. As observed in Fig. 6, the maximum of fluctuations is located in the middle of the boundary layer (at $z/\delta \sim 0.6$) in the relaxation zone. Nevertheless, one can note the presence of a second fluctuation peak at the end of the computational domain (at $x = 420$ mm) in the near-wall region. This testifies of a progressive return to the canonic boundary layer. The differences between different test cases are relatively weak. However, one can remark that the velocity fluctuations for case D are slightly overestimated with respect to other computations and LDA measurements. Furthermore, the influence of the 6-mm offset appears to be modest because fluctuation profiles vary slowly in the direction of the flow. Globally, the agreement between computations and experiment is very satisfactory for longitudinal velocity fluctuations; this constitutes an encouraging point for LES.

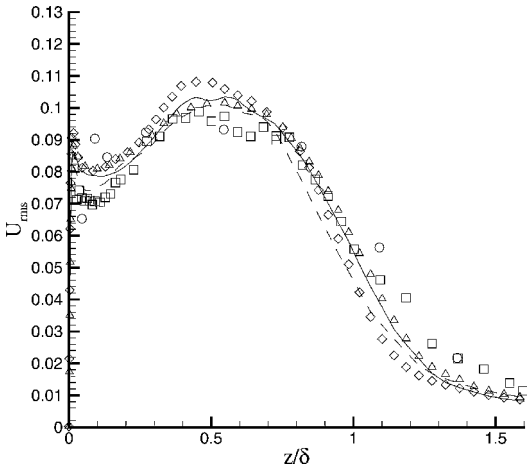

Fig. 13 Mean longitudinal velocity fluctuations profile at x = 420 mm: ——, case A; △, case B; – – –, case C; ◇, case D; ○, HWA; and □, LDA.

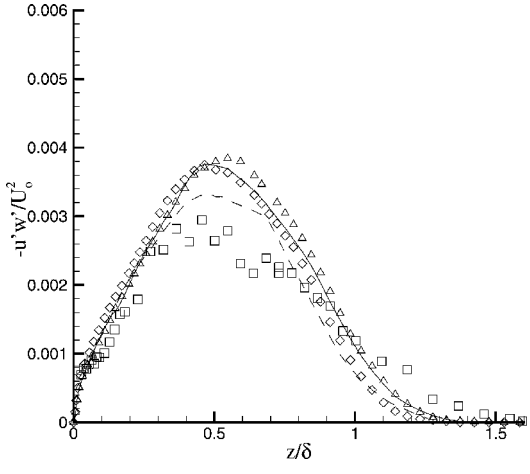

Fig. 14 Mean cross-term tensor ($u'w'$) profile at x = 420 mm: ——, case A; △, case B; – – –, case C; ◇, case D; and □, LDA.

Mean cross-term tensor ($u'w'$) is given in Fig. 14 for the station $x = 420$ mm. It is possible to identify this quantity to the production of turbulent kinetic energy. [In reality, the production term is $-u'w'(\partial u/\partial z)$, but mean velocities are close enough in computations and experience to allow this identification.] Looking at these profiles, one can observe an overestimation of the turbulent production in all simulations with respect to experimental data. This overestimation reaches 30% for cases A, B, and C. Nevertheless, experimental biases are known to be larger for cross terms than for longitudinal fluctuations, and they lead to an underestimation of the $u'w'$ stress.[38] As for longitudinal fluctuations, $u'w'$ is maximum in the middle of the boundary layer both for computations and experiments. Case C (with the best resolution in the longitudinal direction) introduces the weakest discrepancies with respect to experiments (about 15% error).

E. Temporal Signal Analysis

Temporal signals extracted from case A have been analyzed by P. Dupont at IRPHE. Wavelet transform has been used. Comparisons are presented for a station near the outflow ($x = 420$ mm) at $z = 10$ mm. Figure 15 displays kinetic energy spectrum density computed by means of a wavelet transform for the same number of samples (4096) for both experiment and computation. This sample number is considered to be very low by experimentalists, and the description of low frequency is then subject to caution. Nevertheless, for frequency larger than 10 kHz the agreement between computation and experiment is very satisfactory.

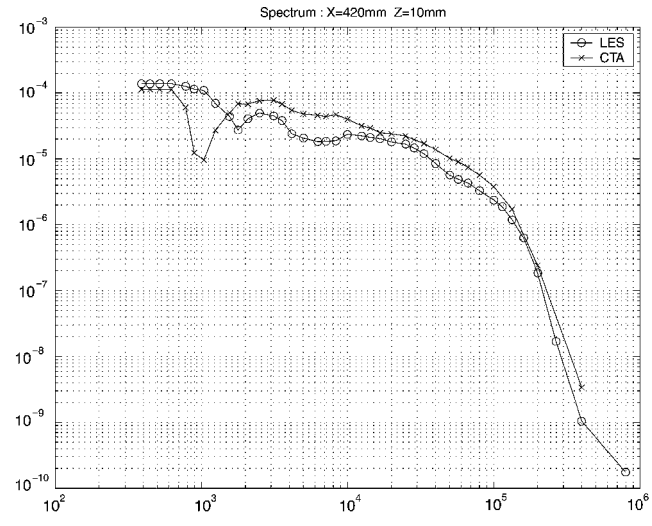

Fig. 15 Kinetic energy spectral density. Wavelet transform with the same number of sample for case A and for experiment.

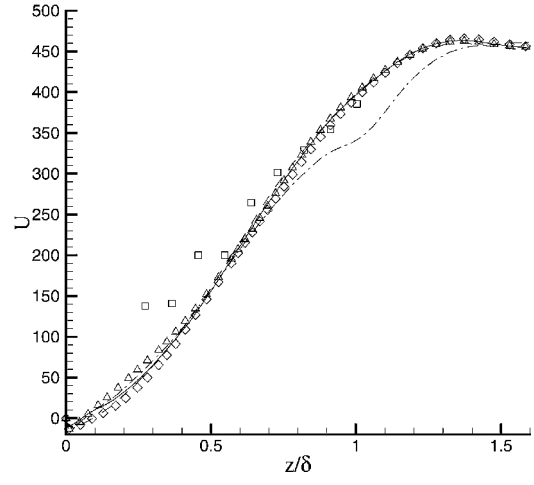

Fig. 16 Mean longitudinal density profile. At x = 326 mm: ——, case A; △, case B; – – –, case C; and ◇, case D. At x = 320 mm: –·–, case A and □, LDA.

F. Description of the Interaction Zone

Mean and fluctuating longitudinal velocity profiles are given in Figs. 16 and 17, respectively. As for profiles downstream of the interaction, a downstream offset of 6 mm is also introduced for cases A, B, C, and D (which are then traced for $x = 326$ mm). To evaluate the effect led by this offset, results for case A at $x = 320$ mm are reported in both figures. The separated zone experimentally measured spreads from $x = 300$ to 332 mm, and the thickness of the separation reaches 1.5 mm at $x = 316$ mm. So, Figs. 16 and 17 concern a region where the separation is maximum (which can be verified looking at Fig. 5). In this zone the measurement difficulties are very important, and despite some significant discrepancies in the near-wall region for the mean velocity profile (Fig. 16) the agreement between computation and experiment is found satisfactory. One can note on computed profiles that the negative mean velocity reaches about 15 m/s. Furthermore, one can estimate comparing case A results for $x = 320$ and 326 mm that the offset of 6 mm is relevant.

For longitudinal velocity fluctuation the agreement between computations and experiments is found satisfactory (Fig. 17). Differences between four test cases are not significant despite some difference for the friction coefficient in particular. However, the case A resolution and size of the computational domain are found sufficient to avoid major numerical dependences.

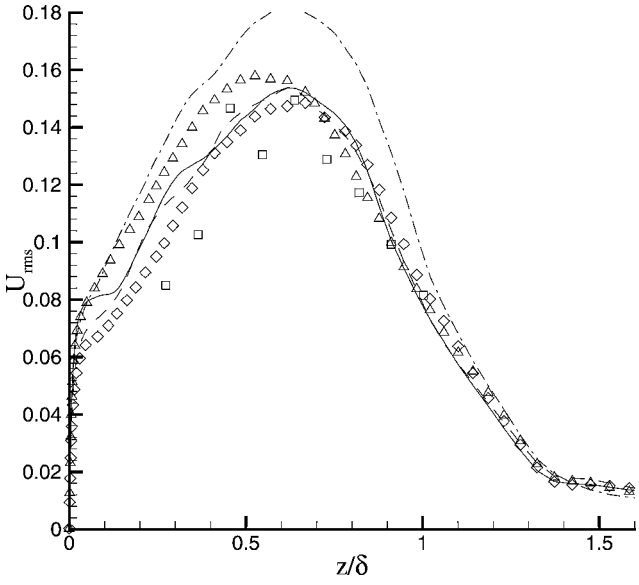

Fig. 17 Longitudinal velocity fluctuations profile. At $x = 326$ mm: ——, case A; △, case B; – – –, case C; and ◇, case D. At $x = 320$ mm: –·–, case A and □, LDA.

V. Conclusions

Bidimensional interaction and oblique shock with a plane plate have been studied numerically using LES and compared with experimental data. This case constitutes a challenge for LES. Numerical results are in quantitative agreement with experimental results, and LES can now be considered as a predictive tool for such physically complex flow. Mean and fluctuating longitudinal velocity are in very satisfactory agreement with experimental data. Nevertheless, cross term ($u'w'$) appears underestimated. The separated zone is correctly described, and LES can be used for fine study of the physics of such an interaction. The numerical dependence of the solution has been studied extensively. The effects of the size of the domain in the spanwise direction, of the resolution in the longitudinal direction, and the presence of a SGS model do not appear to be deciding. One can note an effect of the absence of SGS model on the friction coefficient. However, one can consider that the resolution of case A is sufficient to avoid major dependence to numerical parameters. The No-SGS case can be related to a monotonic integrated large eddy simulation (MILES) approach in the sense that the only dissipation introduced in this computation is the one of the numerical scheme. Nevertheless, in all MILES computations to date a residual level of numerical dissipation is kept, whereas in these LES the numerical dissipation is canceled in most of the boundary layer thanks to the Ducros et al.[19] sensor. Whereas true MILES computations have not been considered in this study, we can expect that good results can be obtained using this approach if the resolution is comparable to the one of case A. The treatment of the inflow conditions is another satisfactory point. Finally, longer integration would have been necessary to obtain a better description of the low frequencies. This work opened the way to the use of compressible LES for both physically and geometrically complex flows. Nevertheless, some issues concerning high-precision numerical schemes in complex geometry remain to be investigated.

Acknowledgments

The authors would like to acknowledge P. Dupont at the Institut de Recherche pour les Ecoulements Hors Equilibre for his contribution to the analysis of the temporal signal extracted from the computations. This work was financially supported by the Délégation Génerale pour l'Armement/Service des Programmes Aéronautiques, French Ministry of Defense.

References

[1]Adamson, T. C., and Messiter, A. F., "Analysis of Two-Dimensional Interaction Between Shock Waves and Boundary Layers," *Annual Review of Fluid Mechanics*, Vol. 12, 1980, pp. 103–138.

[2]Delery, J., and Marvin, G. J., "Shock-Wave Boundary Layer Interactions," AGARDograph 280, Feb. 1986, pp. 51–55.

[3]Smits, A. J., and Dussauge, J. P., *Turbulent Shear Layers in Supersonic Flow*, AIP Press, Woodbury, NY, 1996, pp. 285–319.

[4]Settles, G. S., and Dodson, L. J., "Supersonic and Hypersonic Shock/Boundary-Layer Interaction Database," *AIAA Journal*, Vol. 32, No. 7, 1994, pp. 1377–1383.

[5]David, E., "Modélisation des Écoulements Compressibles et Hypersoniques," Ph.D. Dissertation, Dept. of Engineering, Grenoble Univ., Grenoble, France, June 1993.

[6]Hunt, D., and Nixon, D., "A Very Large Eddy Simulation of an Unsteady Shock Wave/Turbulent Boundary Layer Interaction," AIAA Paper 95-2212, June 1995.

[7]Adams, N. A., "Direct Simulation of the Turbulent Boundary Layer Along a Compression Ramp at $M = 3$ and $Re_\theta = 1685$," *Journal of Fluid Mechanics*, Vol. 420, No. 1, 2000, pp. 47–83.

[8]Urbin, G., Knight, D., and Zheltovodov, A. A., "Compressible Large Eddy Simulation using Unstructured Grid: Supersonic Turbulent Boundary Layer and Compression Corner," AIAA Paper 99-0427, Jan. 1999.

[9]Urbin, G., Knight, D., and Zheltovodov, A. A., "Large Eddy Simulation of a Supersonic Compression Corner Part I," AIAA Paper 2000-0398, Jan. 2000.

[10]Liou, W. W., Huang, G., and Shih, T.-H., "Turbulence Model Assessment for Shock Wave/Turbulent Boundary-Layer Interaction in Transonic and Supersonic Flows," *Computers and Fluids*, Vol. 29, No. 3, 2000, pp. 275–299.

[11]Rizetta, D. P., "Evaluation of Explicit Algebraic Reynolds-Stress Models for Separated Supersonic Flows," *AIAA Journal*, Vol. 36, No. 1, 1998, pp. 24–30.

[12]Gleize, V., Schiestel, R., and Couaillier, V., "Multiple Scale Modeling of Turbulent Nonequilibrium Boundary Layer Flows," *Physics of Fluids*, Vol. 8, No. 10, 1996, pp. 2716–2732.

[13]Marshall, T. A., and Dolling, T. S., "Computation of Turbulent, Separated, Unswept, Compression Ramp interactions," *AIAA Journal*, Vol. 30, No. 8, 1992, pp. 2056–2065.

[14]Deleuze, J., "Structure d'une Couche Limite Turbulente Soumise à une Onde de Choc Incidente," Ph.D. Dissertation, Département de Mécanique, Univ. Aix-Marseille II, May 1995.

[15]Laurent, H., "Turbulence d'une Interaction Onde de Choc/Couche Limite sur une Paroi Adiabatique ou Chauffée," Ph.D. Dissertation, Département de Mécanique, Univ. Aix-Marseille II, Sept. 1996.

[16]Garnier, E., Mossi, M., Sagaut, P., Comte, P., and Deville, M., "On the Use of Shock-Capturing Scheme for Large-Eddy Simulation," *Journal of Computational Physics*, Vol. 153, No. 2, 1999, pp. 273–311.

[17]Yee, H. C., Sandham, N. D., and Djomehri, M. J., "Low-Dissipative High-Order Shock-Capturing Methods Using Characteristic-Based Filters," *Journal of Computational Physics*, Vol. 150, No. 1, 1999, pp. 199–238.

[18]Garnier, E., Sagaut, P., and Deville, M., "A Class of Explicit ENO Filters with Applications to Unsteady Flows," *Journal of Computational Physics*, Vol. 170, No. 1, 2001, pp. 184–204.

[19]Ducros, F., Ferrand, V., Nicoud, F., Weber, C., Darracq, D., Gacherieu, C., and Poinsot, T., "Large-Eddy Simulation of Shock/Turbulence Interaction," *Journal of Computational Physics*, Vol. 152, No. 2, 1999, pp. 517–549.

[20]Garnier, E., Sagaut, P., and Deville, M., "Large-Eddy Simulation of Shock/Homogeneous Turbulence Interaction," *Computers and Fluids*, Vol. 31, No. 2, 2002, pp. 245–268.

[21]Speziale, C. G., Erlebacher, G., Zang, T. A., and Hussaini, M. Y., "The Subgrid-Scale Modeling of Compressible Turbulence," *Physics of Fluids*, Vol. 31, No. 4, 1988, pp. 940–942.

[22]Lee, S., "Large-Eddy Simulation of Shock Turbulence Interaction," *Center for Turbulent Research, Annual Research Briefs 1992*, Stanford Univ., Stanford, CA, 1993, pp. 73–84.

[23]Vreman, B., Geurts, B., and Kuerten, H., "A Priori Tests of Large Eddy Simulation of the Compressible Plane Mixing Layer," *Journal of Engineering Mathematics*, Vol. 29, March 1995, pp. 299–327.

[24]Sagaut, P., *Large Eddy Simulation for Incompressible Flows*, Springer-Verlag, Berlin, 2001, pp. 94, 95.

[25]Lenormand, E., Sagaut, P., Ta Phuoc, L., and Comte, P., "Subgrid-Scale Models for Large-Eddy Simulation of Compressible Wall Bounded Flows," *AIAA Journal*, Vol. 38, No. 8, 2000, pp. 1340–1350.

[26]Lenormand, E., Sagaut, P., and Ta Phuoc, L., "Large-Eddy Simulation of Subsonic and Supersonic Channel Flow at Moderate Reynolds Number," *International Journal for Numerical Methods in Fluids*, Vol. 32, 2000, pp. 369–406.

[27]Erlebacher, G., Hussaini, M. Y., Speziale, C. G., and Zang, T. A., "Toward the Large-Eddy Simulation of Compressible Turbulent Flows," *Journal of Fluid Mechanics*, Vol. 238, No. 1, 1992, pp. 155–185.

[28]Sagaut, P., and Troff, B., "Subgrid-Scale Model Improvements for Non-Homogeneous Flows," *Advances in LES/DNS*, edited by C. Liu and Z. Liu, Greyden, New York, 1997, pp. 401–408.

[29]Moin, P., Squires, K., Cabot, W., and Lee, S., "A Dynamic Subgrid-Scale Model for Compressible Turbulence and Scalar Transport," *Physics of Fluids A*, Vol. 3, No. 11, 1991, pp. 2746–2757.

[30]Shu, C. W., and Osher, S., "Efficient Implementation of Essentially Non-Oscillatory Shock-Capturing Schemes II," *Journal of Computational Physics*, Vol. 83, No. 1, 1989, pp. 32–78.

[31]Jiang, G. S., and Shu, C. W., "Efficient Implementation of Weighted ENO Schemes," *Journal of Computational Physics*, Vol. 126, No. 1, 1996, pp. 202–228.

[32]Guarani, S. E., Moser, R. D., Shariff, K., and Wray, A., "Direct Numerical Simulation of a Supersonic Turbulent Boundary Layer at Mach 2.5," *Journal of Fluid Mechanics*, No. 414, 2000, pp. 1–33.

[33]Thompson, K. W., "Time Dependent Boundary Conditions for Hyperbolic System," *Journal of Computational Physics*, Vol. 68, No. 1, 1987, pp. 1–24.

[34]Lund, T. S., Wu, X., and Squires, K. D., "Generation of Turbulent Inflow Data for Spatially-Developing Boundary Layer Simulations," *Journal of Computational Physics*, Vol. 140, No. 2, 1998, pp. 233–258.

[35]Urbin, G., and Knight, D., "Compressible Large Eddy Simulation Using Unstructured Grid: Unstructured Boundary Layer," *Second AFOSR Conference on DNS/LES*, Kluwer Academic, Norwell, MA, 1999, pp. 443–458.

[36]Spyropoulos, E. T., and Blaisdell, G. A., "Large-Eddy Simulation of a Spatially Evolving Supersonic Turbulent Boundary-Layer Flow," *AIAA Journal*, Vol. 32, No. 11, 1998, pp. 1983–1990.

[37]Morkovin, M. V., "Effects of Compressibility on Turbulent Flows," *Mécanique de la Turbulence*, edited by A. Favre, Centre National de la Recherche Scientifique, Paris, 1962, pp. 367–380.

[38]Eléna., M., and Lacharme, J.-P., "Experimental Study of a Supersonic Turbulent Boundary Layer Using a Laser Doppler Anemometer," *Journal de Mécanique Théorique et Appliquée*, Vol. 7, No. 2, 1988, pp. 175–190.

[39]Kravchenko, A. G., and Moin, P., "On the Effect of Numerical Errors in Large Eddy Simulations of Turbulent Flows," *Journal of Computational Physics*, Vol. 131, No. 2, 1997, pp. 310–322.

H. M. Atassi
Associate Editor